RESEARCH ARTICLE

pssb
physica status solidi b
www.pss-b.com

Growth of Mn_xAu_{1-x} Films on Cu(001) and Ag(001) Single-Crystal Substrates

Ismet Gelen, Tauqir Shinwari, Ivar Kumberg, Sebastien Elie Hadjadj, Yasser A. Shokr, Evangelos Golias, and Wolfgang Kuch*

The growth, morphology, and structure of Mn_xAu_{1-x} films on Cu(001) and Ag(001) are studied by means of low-energy electron diffraction (LEED), medium-energy electron diffraction, Auger electron spectroscopy, and scanning tunnelling microscopy. Different concentrations x from about 0.5 to 1 and thicknesses from 0.2 to 12.9 ML of Mn_xAu_{1-x} are examined. For several values of x, Mn_xAu_{1-x} exhibits a $c(2 \times 2)$ superstructure pattern on Cu(001) when the total thickness is around or above 0.5 ML. Above 1 ML, LEED patterns of Mn_xAu_{1-x} can be only observed on Ag(001), but not on Cu(001). LEED-I(V) is employed to deduce the vertical interlayer distance for as-grown and post-annealed films on Ag(001). Above 500 K, Ag from the substrate segregates into the films.

1. Introduction

Antiferromagnetic (AFM) materials have received increased attention in recent years due to their importance for future spinelectronic applications.[1–3] The main advantages of AFM materials are that they are more robust against external magnetic fields and exhibit a 2–3 orders of magnitude faster spin dynamics than ferromagnets (FM).[4] Because the magnetic moments cancel on the length scale of atomic distances, the study of their magnetic properties is more difficult than that of ferromagnets. Growing AFM materials together with ferromagnetic ones as epitaxial films on single-crystalline substrates is a way to obtain information

I. Gelen, T. Shinwari, I. Kumberg, S. E. Hadjadj, Y. A. Shokr, E. Golias, W. Kuch
Institut für Experimentalphysik
Freie Universität Berlin
Arnimallee 14, 14195 Berlin, Germany
E-mail: kuch@physik.fu-berlin.de

Y. A. Shokr
Faculty of Science
Department of Physics
Helwan University
17119 Cairo, Egypt

about the AFM magnetic properties from the interaction at the structurally well-defined AFM/FM interface.[5–8]

Mn_2Au is an AFM material that is very attractive for spintronic applications[9] because of its noncentrosymmetric spin structure with respect to the lattice, which allows for current-induced realignment of the AFM spin axis.[10] Due to its very high Néel temperature (T_N) above 1000 K[11–16] and concurrent thermal stability, Mn_2Au is also a promising candidate for applications such as a pinning layer in giant magnetoresistance devices,[17] an electrically switchable AFM material,[18] or a spin valve.[19]

Bulk Mn_2Au has a tetragonal body-centered crystal structure with lattice constants $a = 3.33$ Å and $c = 8.54$ Å,[12,20] and its magnetic easy axis is in the $<110>$ direction in the (001) plane.[16] The Mn_2Au AFM domain structure has been investigated by photoemission electron microscopy with X-ray magnetic linear dichroism as contrast mechanism under the influence of current-induced Néel spin–orbit torques.[21] Bommanaboyena et al. prepared 45 nm $Mn_2Au(001)$ on 13 nm $Ta(001)$/$Al_2O_3(1–102)$ both by molecular beam epitaxy (MBE) and rf magnetron sputtering.[22] They found, with the help of atomic force microscopy, that MBE-grown samples show a smoother surface than rf-magnetron-sputtered samples and that for annealing temperatures higher than 450 °C, Mn starts to desorb from the film, which causes a change in the stoichiometry and crystallographic phase.[22] Mn_2Au films have also been prepared by magnetron sputtering on yttrium iron garnet[23] and on MgO(100),[24] which resulted in polycrystalline Mn_2Au films and in (103)-oriented quasiepitaxial films, respectively.

Besides Mn_2Au, many other Mn_xAu_{1-x} bimetallic alloy phases exist as bulk materials that exhibit FM or AFM order, such as FM $MnAu_4$ ($T_C = 361$ K,[11] 373 K[25]), AFM $MnAu_3$ ($T_N = 145$ K), AFM $MnAu_2$ ($T_N = 363$ K,[11] 365 K[25]), AFM $MnAu$ ($T_N = 523$ K,[12] 503 K[26]), and AFM Mn_2Au_5 ($T_N = 353$ K,[11,27] 354 K[28]).

Here, we study the growth and structure of Mn_xAu_{1-x} for x between about 0.5 and 1 on two fourfold-symmetric coinage metal single-crystal surfaces, namely on Cu(001) and Ag(001). The two substrates have both fcc crystal structure, but with different surface lattice constants $a/\sqrt{2}$ of 2.55 and 2.88 Å for Cu(001) and Ag(001), respectively. These two single-crystal surfaces have not been used before as a substrate for Mn_xAu_{1-x} films. Growth of both constituents separately, however, has been studied previously on Cu(001)[29–38] and can be compared to our

results. The metallic substrates allow us to study the initial stages of growth by scanning tunnelling microscopy (STM). We follow the growth morphology by medium-energy electron diffraction (MEED) during deposition and investigate the structure of the films by low-energy electron diffraction (LEED). Auger electron spectroscopy (AES) is employed to determine the alloy composition x and cross-check the film thickness. The results reveal that on Cu(001), although the MEED intensity exhibits layer-wise oscillations during deposition indicative of layer-by-layer growth, multilayer thicknesses of Mn_xAu_{1-x} do not display any structural long-range order in LEED. On Ag(001), in contrast, the films grow epitaxially layer by layer in a *bct* lattice up to the maximum thickness of 12.9 monolayers (ML) studied here.

2. Results

2.1. Mn_xAu_{1-x} on Cu(001)

STM was employed to study the evolution of the morphology of Mn_xAu_{1-x} deposited on Cu(001) at room temperature for different concentrations x. **Figure 1** presents STM images of the clean Cu(001) surface and for different coverages of Mn_xAu_{1-x} on Cu(001) from 0.19 to 2.26 ML. The graphs on the right-hand side present the corresponding height profiles, taken along the white lines in the STM images. At submonolayer coverages, the MnAu coverage was determined by measuring the percentage of surface covered by islands. At higher coverages, MEED intensity oscillations as will be discussed further down were used for coverage determination. The STM image of clean Cu(001) in Figure 1a shows wide terraces with single-monolayer steps, as confirmed in the corresponding line scan along the white line in Figure 1k. Small flat islands of monolayer height with rounded shape are formed at the initial stages of growth of Mn_xAu_{1-x} on Cu(001). These islands merge and grow laterally in size with increasing coverage. However, also at higher submonolayer coverages, some smaller islands still exist. Within x in the range from 0.65 to 1, we cannot observe any clear impact of x on island formation and shape. When the coverage reaches 1 ML, the whole surface is extremely smooth, as seen in Figure 1i.
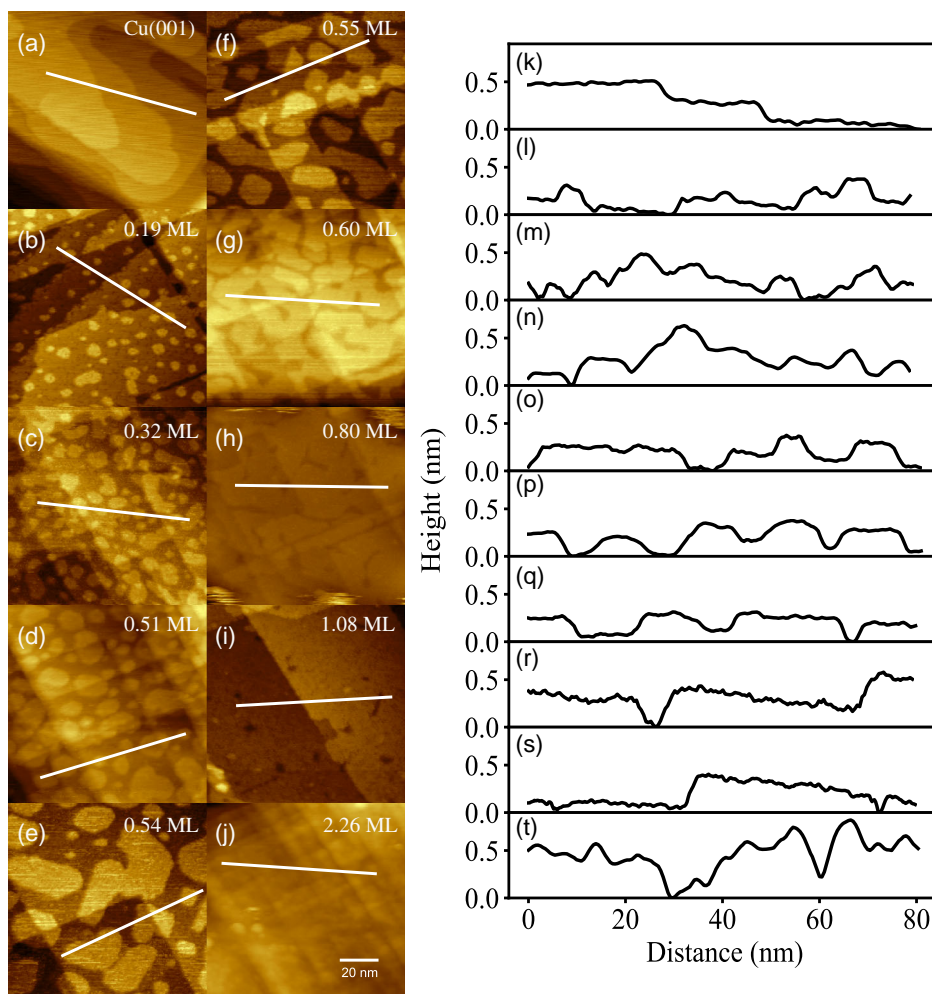

Figure 1. a) STM topography image of Cu(001). STM topography images of b) 0.19 ML $Mn_{0.9}Au_{0.1}$, c) 0.32 ML Mn, d) 0.51 ML $Mn_{0.95}Au_{0.05}$, e) 0.54 ML $Mn_{0.90}Au_{0.10}$, f) 0.55 ML $Mn_{0.65}Au_{0.35}$, g) 0.60 ML Mn, h) 0.80 ML $Mn_{0.77}Au_{0.23}$, i) 1.08 ML $Mn_{0.85}Au_{0.15}$, and j) 2.26 ML $Mn_{0.84}Au_{0.16}$ alloys on Cu(001). STM feedback parameters are a) 0.7 nA, 1 V, b) 1.15 nA, 0.5 V, c) 1.18 nA, 0.5 V, d) 1.19 nA, 0.5 V, e) 1.2 nA, 0.5 V, f) 1.19 nA, 0.5 V, g) 1.14 nA, 0.2 V, h) 1.16 nA, 0.5 V, i) 1.18 nA, 0.2 V, and j) 0.48 nA, 1.2 V. k–t) are line scans along the white lines in (a–j), respectively.

However, at coverages above 1 ML, the films quickly develop a high roughness of more than 0.5 nm with lateral feature sizes below 2 nm, as seen in Figure 1j,t for 2.26 ML $Mn_{0.84}Au_{0.16}$.

The corresponding LEED patterns in the submonolayer regime of Mn_xAu_{1-x} are shown in **Figure 2** for an electron beam energy of 110 eV. The LEED pattern of clean Cu(001) is also presented; here the electron energy is 132.5 eV. It shows a sharp LEED pattern, which corresponds to the smooth surface seen by STM. At submonolayer coverages, the LEED patterns are still influenced by scattering from the substrate. Anyway, no broadening of the spots is observed at any of the submonolayer coverages. What can be observed, though, is the development of a c(2×2) superstructure at coverages above 0.55 ML, which seems to be independent of x within the studied range. For pure Mn films ($x = 1$) on Cu(001), this has been observed before for 0.5 ML Mn grown on Cu(001) at room temperature[29–34] and was assigned to the formation of an ordered Mn–Cu surface alloy, which was also found in density-functional theory calculations.[32]

We suggest that also in the case of Mn_xAu_{1-x} with x larger than 0.65, some kind of 2×2 surface alloy is formed.

When the film thickness exceeds 1 ML, the roughness of the films increases and the LEED patterns disappear. **Figure 3** shows LEED images of 2.07 ML $Mn_{0.82}Au_{0.18}$ and 2.26 ML $Mn_{0.84}Au_{0.16}$ on Cu(001). While for 2.07 ML still some weak LEED spots can be discerned, the 2.26 ML sample does not show any LEED pattern. We interpret this as missing long-range order in the small structures that form at the surface of these films after the completion of the first ML. The investigated samples, their coverage, concentration x, and resulting LEED periodicity are summarized in **Table 1**.

Surprisingly, the alloy films exhibit oscillations of the MEED intensity during deposition at thicknesses above 1 ML. **Figure 4** shows the intensity of the specularly reflected (00) spot as a function of time, converted to thickness in ML, during deposition of Mn_xAu_{1-x} on Cu(001) with x around 0.85, including the two samples as measured in Figure 3. The thickness has been

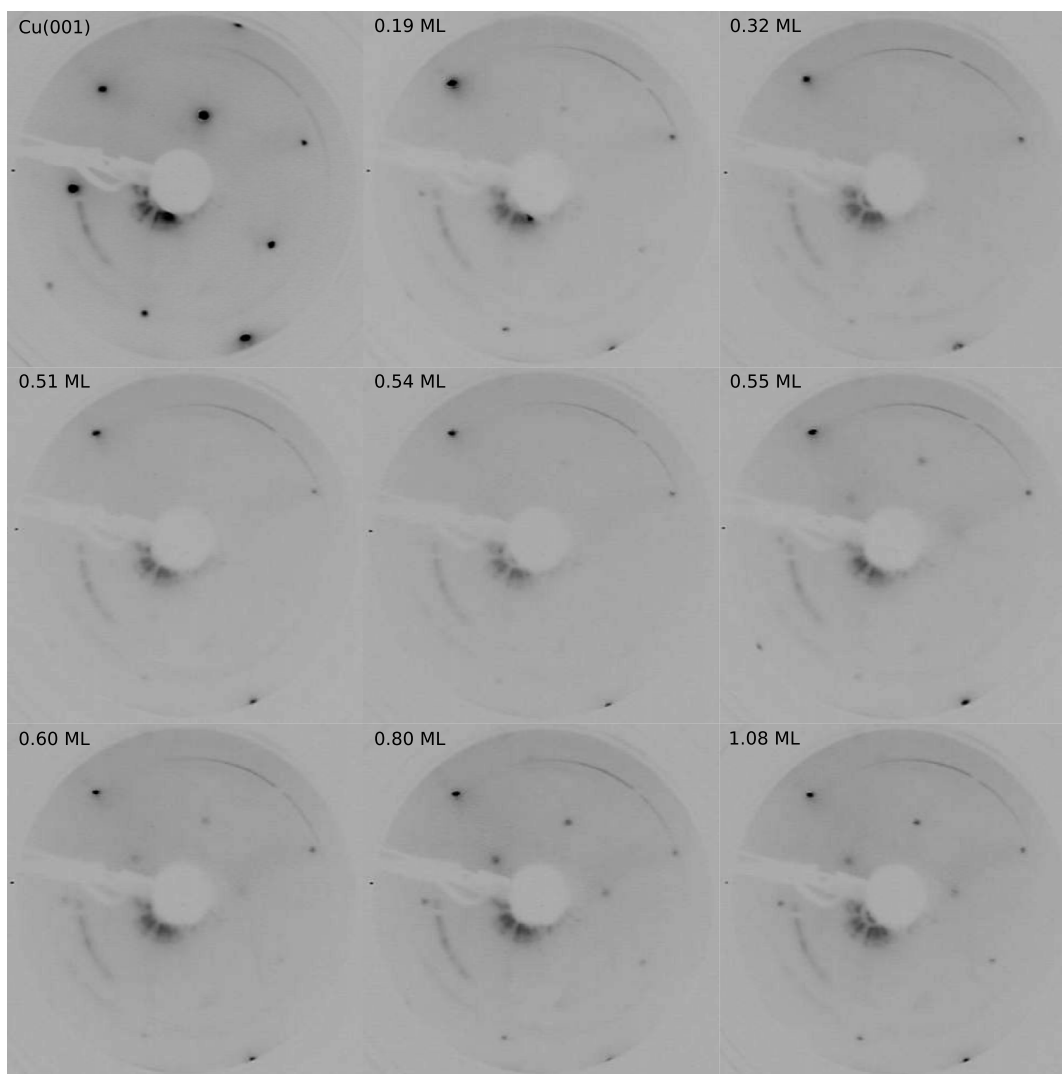**Figure 2.** LEED patterns of clean Cu(001) (132.5 eV electron energy) and Mn_xAu_{1-x} films on Cu(001) for the same samples as in Figure 1b–i at an electron energy of 110 eV.

2300518 (3 of 9)
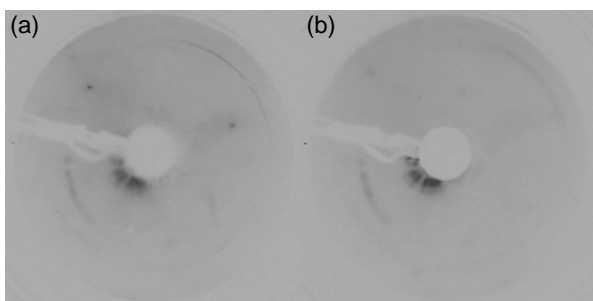
Figure 3. LEED images of a) 2.07 ML $Mn_{0.82}Au_{0.18}$ on Cu(001) at 110 eV. b) 2.26 ML $Mn_{0.84}Au_{0.16}$ on Cu(001) at 180.4 eV.

Table 1. Coverage, composition x, and LEED results of the investigated Mn_xAu_{1-x} films on Cu(001). Coverages below 1 ML have been determined from STM images, above 1 ML from MEED oscillations. x is obtained from AES spectra.

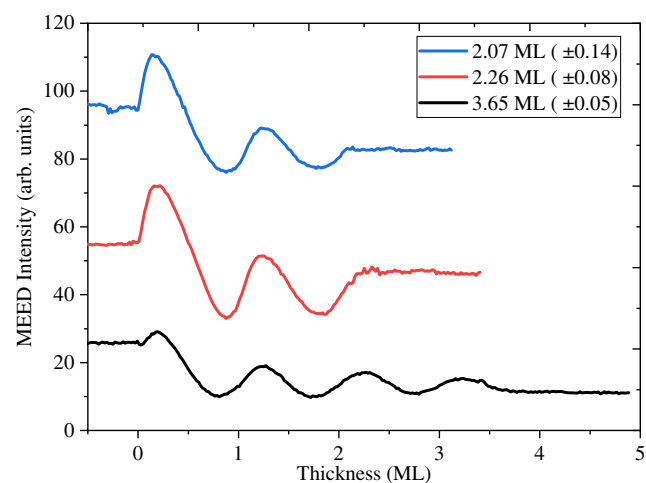| Sample	Coverage [ML]	x	LEED
Figure 1b	0.19 ± 0.02	0.90 ± 0.50	1×1
Figure 1c	0.32 ± 0.04	1.00	1×1
Figure 1d	0.51 ± 0.07	0.95 ± 0.30	1×1
Figure 1e	0.54 ± 0.08	0.90 ± 0.30	1×1
Figure 1f	0.55 ± 0.08	0.65 ± 0.40	$c(2 \times 2)$
Figure 1g	0.60 ± 0.09	1.00	$c(2 \times 2)$
Figure 1h	0.80 ± 0.12	0.77 ± 0.25	$c(2 \times 2)$
Figure 1i	1.08 ± 0.16	0.85 ± 0.15	$c(2 \times 2)$
Figure 3a	2.07 ± 0.14	0.82 ± 0.05	Faint 1×1
Figure 1j	2.26 ± 0.08	0.84 ± 0.05	None
Figure 3b	3.65 ± 0.05	0.85 ± 0.05	None

Figure 4. MEED specular (00) spot intensity versus time, calibrated in thickness, for the deposition of 2.07 ML $Mn_{0.82}Au_{0.18}$, 2.26 ML $Mn_{0.84}Au_{0.16}$, and 3.65 ML $Mn_{0.85}Au_{0.15}$ on Cu(001). The growth rates for 2.07, 2.26, and 3.65 ML are around 58, 53, and 49 s/ML, respectively. The curves are shifted vertically for clarity.

calculated by assuming that the time between adjacent maxima of the MEED oscillations corresponds to the deposition time of 1 ML.

MEED refers to the diffraction of electrons incident to the sample under grazing incidence. The intensity of the diffraction spots is thus sensitive to surface roughness, but depends also on electron diffraction. The initial increase in MEED intensity in Figure 4 upon start of the deposition indicates that the intensity is not purely representing the surface roughness of the sample but is influenced also by electron diffraction. Since the azimuthal angle of the sample in the MEED experiment could not be changed to adjust to a maximum of diffracted intensity of the clean substrate, an increase in intensity resulting from the different vertical lattice spacing of the film compared to the substrate may be superimposed to the intensity oscillations from the surface roughness.

MEED oscillations are an indication of layer-by-layer growth. While pure Mn does not exhibit MEED oscillations on Cu(001), it does show oscillations on $Cu_3Au(001)$.[39] In the case of Mn_xAu_{1-x} on Cu(001) with x around 0.85, we have the situation that although there are no LEED patterns, which indicates the absence of long-range crystallographic order in the films, MEED shows intensity oscillations with monolayer periodicity. One explanation could be that on top of the first, flat monolayer of Cu–Mn–Au alloy, which grows epitaxially with the lateral lattice constant of Cu(001), there is local layer-by-layer growth of Mn–Au, which then, due to the large lattice mismatch to Cu(001), exhibits only short-range lateral crystallographic order.

2.2. Mn_xAu_{1-x} on Ag(001)

In this section, we will now discuss the growth and structure of Mn_xAu_{1-x} on Ag(001). **Figure 5**a shows an STM image of 1.7 ML $Mn_{0.83}Au_{0.17}$ on Ag(001), deposited at room temperature. The surface of the sample exhibits flat areas with steps in between, holes, grooves, and islands. Figure 5b presents a line scan along the white line in panel (a). One can see that the features in the STM image are of single-atomic height. The LEED pattern of the same sample, shown in Figure 5c, presents a $p(1\times1)$ pattern.

Figure 6 displays the MEED intensity during the deposition of 6.4 ML $Mn_{0.71}Au_{0.29}$, 11.4 ML $Mn_{0.43}Au_{0.57}$, and 12.9 ML $Mn_{0.72}Au_{0.28}$ on Ag(001). Oscillations are visible up to at least around 12 ML, indicative of layer-by-layer growth of Mn_xAu_{1-x} on Ag(001) at room temperature. The amplitude of the oscillations decreases after about 5 ML. The initial increase in intensity after opening the shutter of the evaporator may again be attributed to the impossibility to adjust the clean substrate to maximum constructive diffraction conditions of the (00) spot.

The structure of several Mn_xAu_{1-x} films on Ag(001) was studied by LEED. By recording the intensity of the (00) spot as a function of electron energy (LEED-I(V)), a simple kinematic approach allows to extract the average vertical lattice spacing. The result for clean Ag(001), Mn films (from 3.4 to 11.7 ML) on Ag(001), and Mn_xAu_{1-x} films (from 5 to 12.9 ML) on Ag(001) for different Mn-Au ratios x between 0.30 and 0.98 is shown in **Figure 7**. Above about 5 ML film thickness, diffraction from the Ag substrate does not play a role anymore. It is observed that the vertical interlayer distance of pure Mn films is $\approx1.8–1.9$ Å, slightly
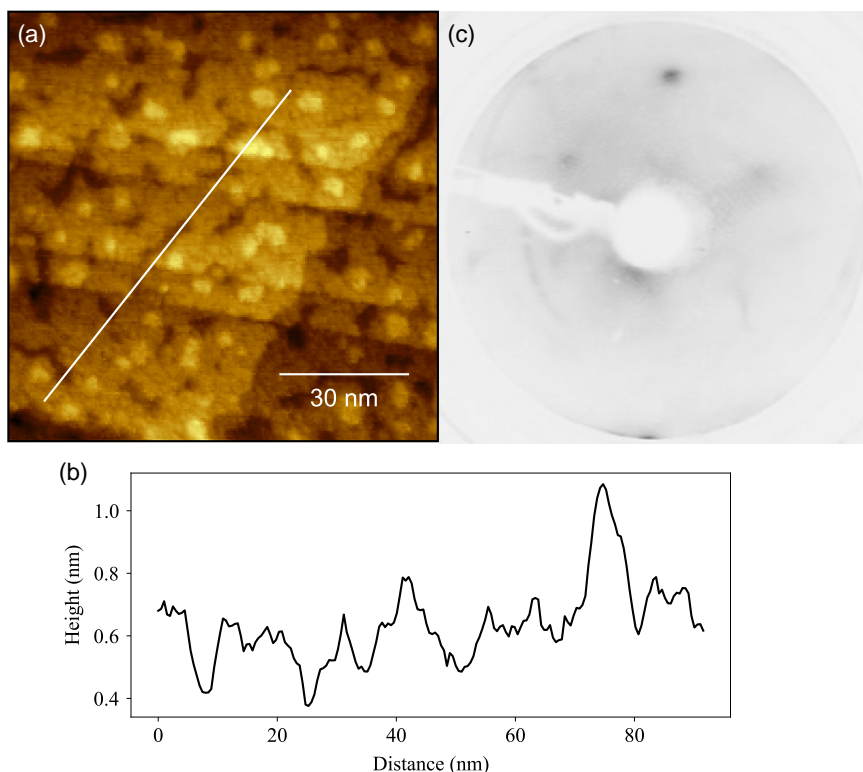
Figure 5. a) STM topography image of 1.7 ML $Mn_{0.83}Au_{0.17}$ on Ag(001), STM feedback parameters 0.49 nA, 1 V. b) Line scan along the white line in (a). c) LEED image of the same sample, electron energy 90 eV.
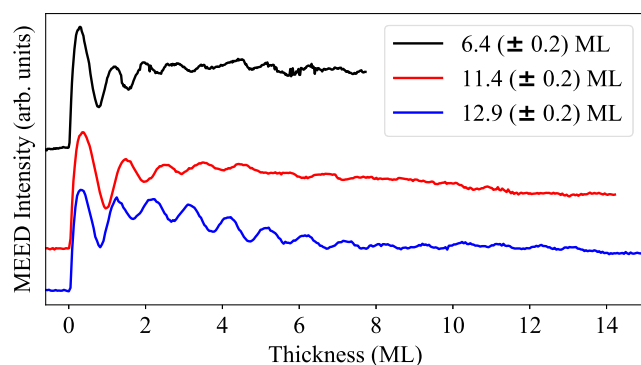

Figure 6. MEED specular (00) spot intensity versus time, calibrated in thickness, for the deposition of 6.4 ML $Mn_{0.71}Au_{0.29}$, 11.4 ML $Mn_{0.43}Au_{0.57}$, and 12.9 ML $Mn_{0.72}Au_{0.28}$ on Ag(001). The growth rates for 6.4, 11.4, and 12.9 ML are around 47, 26, and 23 s/ML, respectively. The curves are shifted vertically for clarity.

Figure 7. Vertical interlayer distance obtained from a kinematic analysis of the LEED-I(V), comparison for the clean Ag(001) substrate (triangle), Mn films (stars), and Mn_xAu_{1-x} films (bullets) on Ag(001). The Mn concentration x for the latter is color-coded into the symbols according to the legend shown at the right-hand side.

smaller than the vertical interlayer distance of Ag(001). With increasing Au content in Mn_xAu_{1-x} films on Ag(001), the vertical interlayer distance increases up to around 2.0 Å, close to the vertical interlayer distance of Ag(001).

Figure 8 shows LEED images of Ag(001) and three Mn_xAu_{1-x} films on Ag(001). The as-grown films, 12.9 ML $Mn_{0.72}Au_{0.28}$ (c), 11.4 ML $Mn_{0.43}Au_{0.57}$ (e), and 6.4 ML $Mn_{0.71}Au_{0.24}$ on Ag(001) (g), display $c(2 \times 2)$ superstructure spots. These superstructure spots disappear after post-annealing the films to above 500 K for a
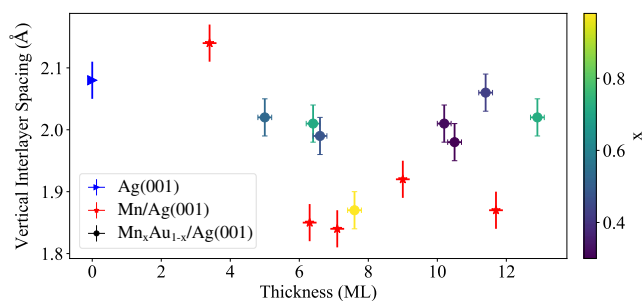
few minutes, as shown in Figure 8d,f,h. At the same time, the (1×1) spots become more intense.

To illustrate the changes occurring by post-annealing, we present LEED-I(V) curves and AES spectra in **Figure 9**. Panel (a) compares the LEED-I(V) curve of the clean Ag(001) substrate (blue) with the one of as-grown 12.9 ML $Mn_{0.72}Au_{0.28}$ on Ag(001) (black) and after 3 min of post-annealing at 600 K (red). The respective AES spectra are displayed in Figure 9b. It is evident that the LEED-I(V) curves after post-annealing are virtually identical to the ones of clean Ag(001), while the curve of the as-grown sample is characteristically different. The AES spectrum after
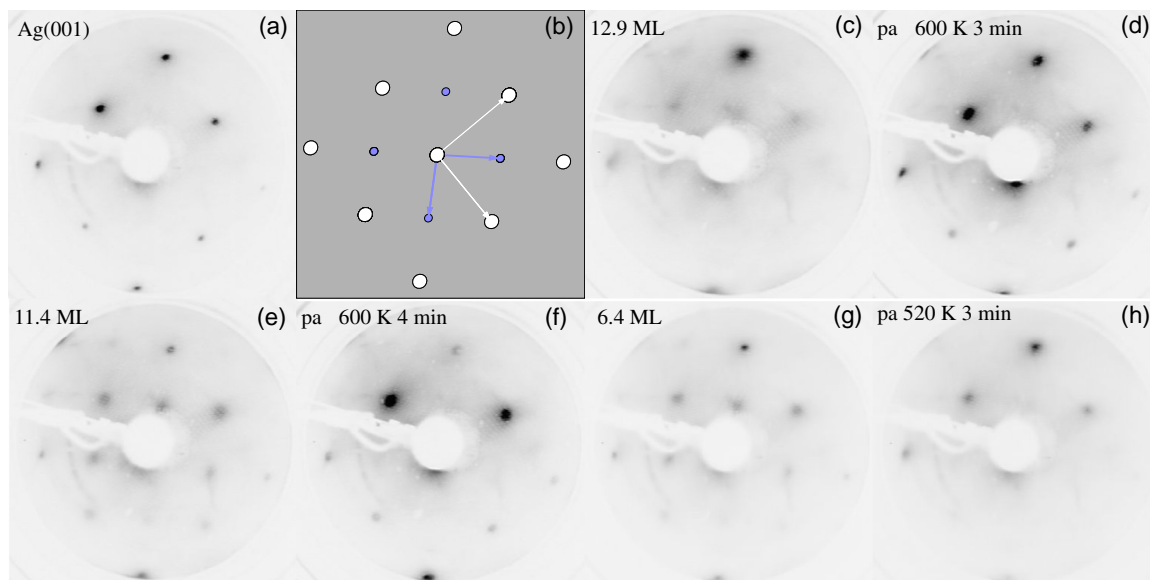
Figure 8. LEED images of Ag(001) a) and of as-grown and post-annealed (pa) Mn_xAu_{1-x} films on Ag(001) (c–h). b) LEED pattern simulated for the $c(2 \times 2)$ superstructure by LEEDpat.[45] White and blue arrows indicate substrate and superstructure spots, respectively. c,d) 12.9 ML $Mn_{0.72}Au_{0.28}$, e,f) 11.4 ML $Mn_{0.43}Au_{0.57}$, g,h) 6.4 ML $Mn_{0.71}Au_{0.29}$. In d,f,h) the samples have been post-annealed at the temperatures and times given in the legends. Electron energy: 100 eV, except e,f): 105 eV.
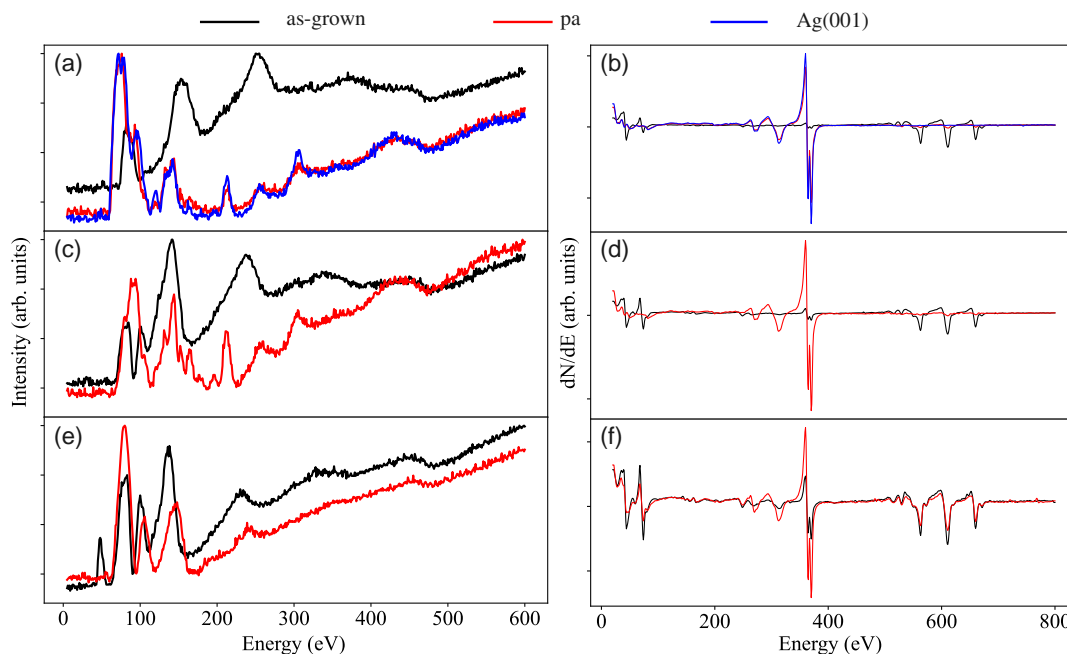

Figure 9. LEED I(V) curves and AES spectra of Mn_xAu_{1-x} on Ag(001). LEED I(V) of a) clean Ag(001), 12.9 ML $Mn_{0.72}Au_{0.28}$ as-grown and after post-annealing (pa) to 600 K for 3 min, c) 11.4 ML $Mn_{0.43}Au_{0.57}$ as-grown and after post-annealing to 600 K for 4 min, e) 6.4 ML $Mn_{0.71}Au_{0.29}$ as-grown and after post-annealing to 520 K for 3 min. b,d,f) shows the corresponding AES spectra to (a,c,e) for the as-grown and post-annealed films, respectively.

post-annealing is characterized by a substantial reduction of the intensity of the Mn *LMM* peaks at 542, 589, and 642 eV and a significant increase of the Ag signals at 250–380 eV, nearly reaching the level of the clean Ag substrate. The low-energy peaks of Mn (40 eV) and Au (69 eV) vanish completely. The same is

observed after annealing 11.4 ML $Mn_{0.43}Au_{0.57}$ for 4 min to 600 K [panels (c) and (d)]. These are clear indications that the MnAu films diffuse into the substrate at these annealing temperatures. Figure 9e,f shows the results for post-annealing 6.4 ML $Mn_{0.71}Au_{0.29}$ on Ag(001) to 520 K for 3 min. Also here the Ag

AES signals increase, but the reduction of the Mn AES intensity is less severe than in the other two samples. The LEED-I(V) curve still resembles the one of the as-deposited film (Figure 9e); however, there is a slight reduction in lattice constant of around 4%. This means that interdiffusion sets in at around 520 K and that the temperature for annealing must be kept below that temperature. Below 500 K, we did not observe any diffusion.

3. Discussion and Conclusion

The aim of this work was to investigate growth, surface structure, and morphology of well-defined ultrathin Mn_xAu_{1-x} films grown on Cu(001) and Ag(001) single-crystal surfaces. Cu and Ag both have an fcc structure, but with different lattice constants. While the nearest-neighbor distance in the (001) surface is 2.88 Å in Ag, it is 2.55 Å in Cu. As seen from Figure 7, the Mn_xAu_{1-x} films are strained when deposited on the Ag(001) surface, with the vertical lattice constant being smaller than the lateral one. The strain seems to get larger with higher Mn concentration. On Cu(001), LEED-I(V) measurements were not feasible, as LEED images were only observed for submonolayer coverages. However, Mn-rich epitaxial NiMn films on Cu(001) adopt a larger out-of-plane lattice spacing compared to that of Cu(001).[40] We assume that this is also the case for Mn_xAu_{1-x}. The films are thus under tensile stress on Ag(001) and under compressive stress on Cu(001). This may explain the different morphologies observed for Mn_xAu_{1-x} films with multilayer thickness on the two substrates.

The c(2 × 2) superstructure observed in LEED for different values of x and thicknesses d in the submonolayer range on both, Cu(001) and Ag(001), may be explained by an intermixing of substrate and film atoms in the topmost surface layer to form a checkerboard array with c(2 × 2) unit cell, similar to what has been observed for 0.5 ML Au grown at room temperature on Cu(001)[35–38] or 0.5 ML Mn grown on Cu(001) at room temperature.[29–34] A c(2 × 2) superstructure has also been reported for MnAu deposited on bct Mn(001) by Yamada et al. who initially deposited 7 ML of Mn on Fe and then Au on top to obtain the MnAu alloy.[41,42]

As shown in Figure 8, we observe c(2 × 2) LEED patterns also for thicker films of Mn_xAu_{1-x} on Ag(001). Here the superstructure spots disappear after post-annealing. This may suggest that the alloy composition at the surface after annealing approaches the one of the interior of the films and removes the $Mn_{0.5}Au_{0.5}$ surface composition, which presumably is responsible for the c(2 × 2) superstructure.

In Mn_xAu_{1-x} on Cu(001), c(2 × 2) superstructure spots are visible in LEED patterns when the coverage exceeds about 0.5 ML (Figure 1). This matches the observation for pure Mn on Cu(001), where a critical coverage of about 0.5 ML of Mn was needed before the ordered Mn–Cu surface alloy formed.[30] We suppose that for our Mn-rich Mn_xAu_{1-x} films on Cu(001), also some islands with a c(2 × 2) surface alloy form when the coverage exceeds 0.5 ML.

STM images display the growth of round-shaped islands with sharp edges of Mn_xAu_{1-x} on Cu(001) at sub-ML coverages. These islands merge to form larger islands and eventually coalesce into a flat 1 ML film. Observed island sizes are between 1.5 and 140 nm². Further deposition of Mn and Au on the 1 ML film leads to a rough surface with no apparent crystalline long-range order, as concluded from the absence of LEED patterns. This behavior, akin to the Stranski-Krastanov growth mode, may be explained by the role of Cu atoms from the substrate surface in the formation of the epitaxial first ML despite the relatively large lattice mismatch, which is then absent in the following atomic layers.

An unexpected observation is that, despite this high roughness and the missing long-range order in thicker Mn_xAu_{1-x} films on Cu(001), still intensity oscillations corresponding to the completion of integer monolayers are observed in the specular MEED intensity (Figure 4). A possible explanation could be local layer-by-layer growth in some Mn-Au patches that exhibit multiple incommensurate crystallographic orientations with respect to each other.

In contrast to Cu(001), epitaxial Mn_xAu_{1-x} films with larger thickness can be grown at room temperature on Ag(001), where we observe layer-by-layer growth, LEED patterns, and a relatively smooth surface as seen by STM. We attribute this difference between the two substrates to the opposite sign of the strain in epitaxial Mn_xAu_{1-x} films. In the case of tensile stress, like in Mn_xAu_{1-x}/Ag(001), vertical buckling is disfavored, which helps in the growth of epitaxial layers, as long as the strain is not too large.

Moderate post-annealing of Mn_xAu_{1-x}/Ag(001) leads to sharper LEED spots and suppresses the c(2 × 2) superstructure. However, already above about 500 K, significant intermixing with Ag substrate atoms occurs, probably favored by the metallic nature of the substrate, its relatively low melting point, and the large atomic radius of Ag compared to Mn. It remains to be seen whether this temperature is high enough to obtain the desired properties such as high T_N and noncentrosymmetric AFM spin structure of ordered Mn_2Au alloys also in these thin films.

To sum up, we have studied the growth of Mn_xAu_{1-x} alloys with $\approx 0.5 \leq x \leq 1$ by MBE on Cu(001) and Ag(001) single-crystal surfaces. While on Ag(001), epitaxial Mn_xAu_{1-x} films grow layer by layer, on Cu(001), in contrast, only a single atomic monolayer shows epitaxial crystalline order. Thicker films on Cu(001) exhibit an increased roughness and do not show LEED patterns. We attribute this to the smaller lattice constant of Cu, which results in too high compressive strain in the films, possibly paired with interdiffusion between film and substrate. On the other hand, Mn_xAu_{1-x}/Ag(001) might be used to interface it with epitaxial ferromagnetic films such as Fe for the study of the magnetic AFM–FM coupling. It might be also interesting to extend the study to Au-rich alloys and to compare the magnetic properties of epitaxial Mn_xAu_{1-x} films to their respective bulk phases.

4. Experimental Section

Cu(001) and Ag(001) single crystals of 10 mm diameter and 2 mm thickness (MaTecK, polished with roughness <0.01 micron and orientation accuracy 0.1 degree) were used as substrates. They were cleaned by several cycles of 1 kV Ar-ion sputtering and annealing at around 900 K for 20 min. Cleanliness and crystallinity of the substrates were verified by AES and LEED, respectively. LEED patterns of the substrates are shown in Figure 2 and 8a for Cu(001) and Ag(001), respectively. The smoothness of the substrates was checked by STM. The topography of the clean

Table 2. LEED-I(V) results for as-grown and post-annealed Mn_xAu_{1-x} on Ag(001). a and b are determined from the Ag356/Mn589 and Mn40/Au69 AES intensity ratios, respectively. The error in the vertical interlayer spacing d_p is ± 0.02 Å.

	As-grown				After post-annealing		
d [ML]	x^a	x^b	d_p [Å]	LEED	T_{ann} [K]	d_p [Å]	LEED
12.9	0.72 ± 0.05	0.76 ± 0.03	2.02	c(2 × 2)	600	2.06	1 × 1
11.4	0.43 ± 0.02	0.69 ± 0.03	2.06	c(2 × 2)	600	2.02	1 × 1
6.4	0.71 ± 0.05	0.76 ± 0.03	2.01	c(2 × 2)	520	1.93	1 × 1

Cu(001) substrate is presented in Figure 1a along with a line profile in Figure 1k.

LEED images and LEED-I(V) curves were taken by a backview LEED system (Omicron SpectaLEED) and recorded by a CCD camera. The room-temperature Omicron STM1 was used to investigate the morphology of the samples by an Fe-ring tip. The Fe ring was prepared as described previously.[43] STM measurements were carried out in constant-current mode at room temperature. The base pressure in the STM chamber was 1×10^{-9} mbar. The samples were transferred between the preparation chamber and the STM chamber without breaking the vacuum. The coverage of submonolayer Mn_xAu_{1-x} films was analyzed from STM images using the Gwyddion software.[44]

Mn_xAu_{1-x} films were deposited at room temperature by co-evaporation of Mn and Au from a 4-pocket evaporator (Oxford, EGN4). Mn flakes (MaTecK, 99.99%) were evaporated from a tantalum crucible, while Au was evaporated by directly heating a Au wire (diameter 1 mm) that was wrapped by a tungsten wire. The base pressure of the preparation chamber was around 5×10^{-10} mbar. During growth, the pressure rose to about 5×10^{-9} mbar.

The MEED measurements were performed by using electrons with 3 keV energy under an incidence angle on the sample of about 5° and monitoring the diffraction pattern on a fluorescence screen by a CCD camera.

In order to determine the concentration x of Mn in the Mn_xAu_{1-x} alloy films, first thick Mn_xAu_{1-x} films were grown on Cu(001) and the MEED oscillations recorded, as shown in Figure 4. Varying the heating power of Mn and keeping the one for Au constant allow to extract the rates for Au and Mn growth separately and to correlate it with AES peak-height ratios. The AES peak intensity ratios of I_{Cu920}/I_{Mn589} and I_{Mn40}/I_{Au70} were then used to obtain the Mn concentration in Mn_xAu_{1-x}. The results along with the uncertainties in x are tabulated in **Table 1** and **2**.

Acknowledgements

Conflict of Interest

The authors declare no conflict of interest.

Data Availability Statement

The data that support the findings of this study are available from the corresponding author upon reasonable request.

[1] T. Jungwirth, X. Marti, P. Wadley, J. Wunderlich, *Nat. Nanotechnol.* **2016**, *11*, 231.

[2] A. B. Shick, S. Khmelevskyi, O. N. Mryasov, J. Wunderlich, T. Jungwirth, *Phys. Rev. B* **2010**, *81*, 212409.

[3] Z. Kašpar, M. Surýnek, J. Zubáč, F. Krizek, V. Novák, R. P. Campion, M. S. Wörnle, P. Gambardella, X. Marti, P. Němec, K. W. Edmonds, S. Reimers, O. J. Amin, F. Maccherozzi, S. S. Dhesi, P. Wadley, J. Wunderlich, K. Olejník, T. Jungwirth, *Nat. Electron.* **2021**, *4*, 30.

[4] A. V. Kimel, A. Kirilyuk, A. Tsvetkov, R. V. Pisarev, T. Rasing, *Nature* **2004**, *429*, 850.

[5] W. Kuch, L. I. Chelaru, F. Offi, J. Wang, M. Kotsugi, J. Kirschner, *Phys. Rev. Lett.* **2004**, *92*, 017201.

[6] U. Schlickum, N. Janke-Gilman, W. Wulfhekel, J. Kirschner, *Phys. Rev. Lett.* **2004**, *92*, 107203.

[7] W. Kuch, L. I. Chelaru, F. Offi, J. Wang, M. Kotsugi, J. Kirschner, *Nat. Mater.* **2006**, *5*, 128.

[8] M. Y. Khan, C.-B. Wu, S. K. Kreft, W. Kuch, *J. Phys.: Condens. Matter* **2013**, *25*, 386005.

[9] X.-T. Jia, X.-L. Cai, W.-Y. Yu, L.-W. Zhang, B.-J. Wang, G.-H. Cao, S.-Z. Wang, H.-M. Tang, Y. Jia, *J. Phys. D: Appl. Phys.* **2020**, *53*, 245001.

[10] J. Železný, H. Gao, A. Manchon, F. Freimuth, Y. Mokrousov, J. Zemen, J. Mašek, J. Sinova, T. Jungwirth, *Phys. Rev. B* **2017**, *95*, 014403.

[11] G. Longworth, B. Window, *J. Phys. F: Met. Phys.* **1971**, *1*, 217.

[12] V. M. T. S. Barthem, C. V. Colin, H. Mayaffre, M. H. Julien, D. Givord, *Nat. Commun.* **2013**, *4*, 2892.

[13] M. Arana, F. Estrada, D. S. Maior, J. B. S. Mendes, L. E. Fernandez-Outon, W. A. A. Macedo, V. M. T. S. Barthem, D. Givord, A. Azevedo, S. M. Rezende, *Appl. Phys. Lett.* **2017**, *111*, 192409.

[14] J. Hirst, U. Atxitia, S. Ruta, J. Jackson, T. Ostler, *Phys. Rev. B* **2022**, *106*, 094402.

[15] S. Selzer, L. Salemi, A. Deák, E. Simon, L. Szunyogh, P. M. Oppeneer, U. Nowak, *Phys. Rev. B* **2022**, *105*, 174416.

[16] S. Reimers, Y. Lytvynenko, Y. R. Niu, E. Golias, B. Sarpi, L. S. I. Veiga, T. Denneulin, A. Kovcs, R. E. Dunin-Borkowski, J. Bläßer, M. Kläui, M. Jourdan, *Nat. Commun.* **2023**, *14*, 1861.

[17] S. Khmelevskyi, P. Mohn, *Appl. Phys. Lett.* **2008**, *93*, 162503.

[18] M. Meinert, D. Graulich, T. Matalla-Wagner, *Phys. Rev. Appl.* **2018**, *9*, 064040.

[19] H.-C. Wu, Z.-M. Liao, R. S. Sofin, G. Feng, X.-M. Ma, A. B. Shick, O. N. Mryasov, I. V. Shvets, *Adv. Mater.* **2012**, *24*, 6374.

[20] P. Wells, J. H. Smith, *Acta Crystallogr. A* **1970**, *26*, 379.

[21] S. Y. Bodnar, M. Filianina, S. Bommanaboyena, T. Forrest, F. Maccherozzi, A. Sapozhnik, Y. Skourski, M. Kläui, M. Jourdan, *Phys. Rev. B* **2019**, *99*, 140409.

[22] S. P. Bommanaboyena, T. Bergfeldt, R. Heller, M. Kläui, M. Jourdan, *J. Appl. Phys.* **2020**, *127*, 243901.

[23] M. Arana, M. Gamino, E. Silva, V. Barthem, D. Givord, A. Azevedo, S. Rezende, *Phys. Rev. B* **2018**, *98*, 144431.

[24] X. Zhou, X. Chen, J. Zhang, F. Li, G. Shi, Y. Sun, M. Saleem, Y. You, F. Pan, C. Song, *Phys. Rev. Appl.* **2019**, *11*, 054030.

[25] S. Abe, M. Matsumoto, H. Yoshida, S. Mori, T. Kanomata, T. Kaneko, *J. Magn. Magn. Mater.* **1992**, *104*, 2059.

[26] G. E. Bacon, E. W. Mason, *Proc. Phys. Soc.* **1967**, *92*, 713.

[27] J. H. Smith, P. Wells, *J. Phys. C: Solid State Phys.* **1969**, *2*, 356.

[28] M. Matsumoto, S. Abe, H. Yoshida, S. Mori, T. Kanomata, T. Kaneko, *J. Magn. Magn. Mater.* **1992**, *104*, 2061.

[29] M. Wuttig, Y. Gauthier, S. Blügel, *Phys. Rev. Lett.* **1993**, *70*, 3619.

[30] H. P. Noh, T. Hashizume, D. Jeon, Y. Kuk, H. W. Pickering, T. Sakurai, *Phys. Rev. B* **1994**, *50*, 2735.

[31] W. L. O'Brien, B. P. Tonner, *Phys. Rev. B* **1995**, *51*, 617.

[32] M. Eder, J. Hafner, E. G. Moroni, *Phys. Rev. B* **2000**, *61*, 11492.

[33] Y. Huttel, C. Teodorescu, F. Bertran, G. Krill, *Phys. Rev. B* **2001**, *64*, 094405.

[34] A. Kimura, S. Asanao, T. Kambe, T. Xie, S. Watanabe, M. Taniguchi, S. Qiao, E. Hashimoto, H. Namatame, T. Muro, S. Imada, S. Suga, *Phys. Rev. B* **2007**, *76*, 115416.

[35] P. W. Palmberg, T. N. Rhodin, *J. Appl. Phys.* **1968**, *39*, 2425.

[36] J. C. Hansen, J. A. Benson, W. D. Clendening, M. T. McEllistrem, J. G. Tobin, *Phys. Rev. B* **1987**, *36*, 6186.

[37] J. C. Hansen, J. G. Tobin, *J. Vac. Sci. Technol. A: Vac. Surf. Films* **1989**, *7*, 2475.

[38] J. G. Tobin, J. C. Hansen, M. K. Wagner, *J. Vac. Sci. Technol. A* **1990**, *8*, 2494.

[39] T. Shinwari, I. Gelen, Y. A. Shokr, I. Kumberg, M. Sajjad, W. Kuch, M. Y. Khan, *Phys. Status Solidi–Rap. Res. Lett.* **2021**, *15*, 2100195.

[40] C. Tieg, W. Kuch, S. G. Wang, J. Kirschner, *Phys. Rev. B* **2006**, *74*, 094420.

[41] T. K. Yamada, R. Robles, E. Martinez, M. M. J. Bischoff, A. Vega, A. L. Vázquez de Parga, T. Mizoguchi, H. van Kempen, *Phys. Rev. B* **2005**, *72*, 014410.

[42] T. K. Yamada, A. L. Vázquez de Parga, M. M. J. Bischoff, T. Mizoguchi, H. van Kempen, *Surf. Sci.* **2006**, *600*, 1048.

[43] C.-B. Wu, J. Song, W. Kuch, *Appl. Phys. Lett.* **2012**, *101*, 012404.

[44] D. Nečas, P. Klapetek, *Open Phys.* **2012**, *10*, 181.

[45] K. Hermann, M. A. Van Hove, LEEDpat4.2: Simulation of LEED Pattern; FHI-Berlin **2023**, https://www.fhi.mpg.de/958975/LEEDpat4.